Journal of Technology Innovations and Energy
https://doi.org/10.56556/jtie.v3i4.1162
ISSN: 2957-8809

RESEARCH ARTICLE

Velocity Slip and Mass Transfer Effects in the magnetohydrodynamic, Upper-Convected Maxwell Fluid Flow Through a Porous Media

Anwar Shahid

School of Software, Quanzhou University of Information Engineering, Quanzhou, 362000, Fujian, P.R. China

Corresponding Author: Anwar Shahid. Email: anwarali@qzuie.edu.cn
Received: 25 October, 2024, Accepted: 28 December, 2024, Published: 30 December, 2024

Abstract
The current investigation elucidates the impact of velocity slip and mass transfer phenomena on the magnetohydrodynamic (MHD) flow of upper-convected Maxwell (UCM) fluids traversing a stretchable porous substrate. The fundamental partial differential equations governing this flow problem are transformed into ordinary differential equations by applying similarity transformations. The numerical solutions for the resultant non-linear boundary value problem are derived by employing the Successive Linearization Method (SLM) utilizing Matlab software. The velocity and concentration profiles for extensive ranges of the governing parametric variables are presented, and their behavior is analyzed through graphical representations. It is anticipated that the results obtained from this study will provide valuable insights for practical applications and will establish connections with existing scholarly literature.

Keywords: Mass transfer; MHD; Stretching sheet; Maxwell Fluid; Porous medium; SLM technique

Introduction

The Earth is replete with a diverse array of examples pertaining to the flow characteristics of non-Newtonian fluids. In recent times, the investigation of such fluids has captivated the attention of researchers and has experienced significant growth over the past two decades. Undoubtedly, the governing equations developed for non-Newtonian fluids are characterized by their strong non-linearity, high order, and complexity, often surpassing that of the Navier-Stokes equations. The flows of non-Newtonian fluids occur across a broad spectrum of applications, including industrial processes such as the production of synthetic fibers, the extrusion of molten plastics, and operations in oil and gas well drilling, as well as certain flow scenarios involving polymer solutions. A vast array of liquids and commercial applications has prompted researchers to explore the behavior of non-Newtonian fluids. Non-Newtonian fluids exhibit distinct properties in comparison to their Newtonian counterparts. It is imperative to examine their flow behavior to gain a comprehensive understanding of non-Newtonian fluids and their applications. Researchers have predominantly focused on the analysis of second and third-grade fluid models, which have not provided adequate predictions regarding the effects of stress relaxation. Anwar et al., (2020) recorded the impact of the ramped wall temperature and ramped wall velocity for an unsteady MHD convective Maxwell fluid flow. MHD Suspended SWCNTs and MWCNTs Based Maxwell Nanofluid Flow with Bio-Convection and Entropy Generation Past a Permeable Vertical Cone were examined by Shah et al. (2020) for their microstructure and inertial characteristics. The MHD swirling flow and heat transfer in

Maxwell fluid powered by two coaxially rotating disks with variable thermal conductivity were investigated by Ahmed et al. (2019), Chen et al. (2019) looked into the unsteady boundary layer flow of a viscoelastic MHD fluid using a double fractional Maxwell model. The forced convective Maxwell fluid flow over a spinning disk under the motion of thermophoretic particles was examined by Shehzad et al. (2020). Various researchers have contributed to the understanding of non-Newtonian fluids through stretchable surfaces in different flow scenarios as evidenced by references (Sami Ullah et al. 2024, Anwar et al. 2020, Anwar et al. (2023).

The MHD flow over a permeable medium plays a significant role in mechanical and agricultural technologies as well as in the extraction of gasoline from fossil fuels in the petroleum industry. MHD tools have found widespread applications in the biomedical and material sciences, and MHD micro-fluids have been widely used in many grasslands. For instance, Daniel et al. (2017) conducted entropy analysis on magnetic hydrodynamic nanomaterial fluid flowing considering radiative chemical reactions and viscous dissipations through numerical methods. They also explored MHD flow adopting the nanofluid model with mixed convection and partial slip conditions, among other variations. Mulinti and Pallavarapu (2022) investigated the flow dynamics of an unsteady compressible magnetohydrodynamic fluid influenced by thermal radiation and situated within a porous subsurface, factoring in the presence of chemical reactions. The works of Wakif et al. (2022), Reddy et al. (2022), and Yahaya et al. (2022) also contributed insights into the influence of MHD and nanofluids under diverse conditions. Recent scholarly discussions have centered on the magnetic hydrodynamic model under specific assumptions, as referenced in works (Mahabaleshwar et al. 2023, Anwar et al. 2022, Alkasasbeh et al. 2023, Anwar et al. 2022). We have demonstrated a strong interest in the analysis of two-dimensional flows for mass transportation in recent years. The mechanisms of heat transmission and fluid flow have significant uses in research and engineering. One constitutive connection between shear stress and rate of strain is insufficient to study the various rheological characteristics of non-Newtonian fluids. Any boundary layer's stress relaxation may be predicted using the Maxwell phenomenon, which also removes the influence of shear-dependent viscosity. An unstable boundary layer is crucial in a number of engineering challenges, including the process of periodic fluid motion and other types brought on by extra time-dependent elements that would impact the fluid motion and boundary layer separation. Makinde (2011) investigated the interaction of thermal radiation, mixed convection, and a chemical reaction. Anwer and Makinde (2011) investigated the species transfer and viscoelastic flow into a Darcian high-porous channel. The peristaltic propulsion for a Jeffrey nanofluid, as well as the effects of thermal radiation and chemical reactions, were investigated by Abbas et al. (2019) The combination of heat and mass transfer for third-grade nanofluids on a stretchy, pervious plate with convective heating was explained in detail by Khan et al. (2015). Through entropy optimization, Deebani et al. (2020) demonstrated the Hall effect on radiative Casson fluid flow via a chemical reaction over a spinning cone. Al-Khaled and Khan (2020) examined the temperature-dependent viscosity and other thermal characteristics of a Casson nanofluid that contained microorganisms. A few pertinent questions on fluid flow and mass transfer over stretched surfaces can be found in (Eid and Mahny 2017, Reddy et al. 2018, Bhatti et al. 2018).

In light of the preceding discourse, the aim of the current research pertaining to the Maxwell fluid model is to delineate the characteristics of non-Newtonian fluid behavior and to scrutinize the influence of velocity slip and mass transfer in magnetohydrodynamic (MHD) upper-convected Maxwell (UCM) fluid flow in the proximity of the stagnation point adjacent to a stretched permeable sublayer. The examination of mass transfer across permeable surfaces holds substantial importance due to its extensive practical applications. The prior studies are grounded in the continuous physical properties of the fluid. The present flow problem is formulated as non-linear ordinary differential equations through the application of suitable similarity transformations and is subsequently solved using the Successive Linearization Method (SLM), yielding significant numerical results (Bhatti et al. 2018, Bhatti et al. 2016, Anwar et al. 2017, Anwar et al. 2018). The methodology currently employed has

demonstrated considerable efficiency and exhibits a rapid convergence rate relative to various numerical approaches. The effects of the governing physical parameter quantities of interest are illustrated through graphical representations and are discussed in detail.

Mathematical Formulation

Let us examine the incompressible, steady stagnation point flow of an upper-convected Maxwell (UCM) fluid that is constrained by a stretched sheet on the specified domain $\bar{y} = 0$. The flow encompasses the defined range $\bar{y} > 0$. An external magnetic field B_0 is applied in a direction transverse to the flow, while the electric and induced magnetic fields are rendered negligible due to the minimal magnetic Reynolds number. Furthermore, the factors influencing mass transfer are also considered. Mass transfer pertains to the flow that incorporates the species A and B, which are only sparingly soluble in the fluid. The concentrations at the surface of the sheet $\tilde{C}_w$, and the solubility of the species in the fluid are delineated, while the concentrations away from the sheet $\tilde{C}_\infty$, are noted, alongside the reaction rate k_1. The velocity magnitudes at the stagnation point are $\bar{x} = 0, \bar{y} = 0$ presented as specified.

The velocity magnitudes of the stagnation point are furnished as

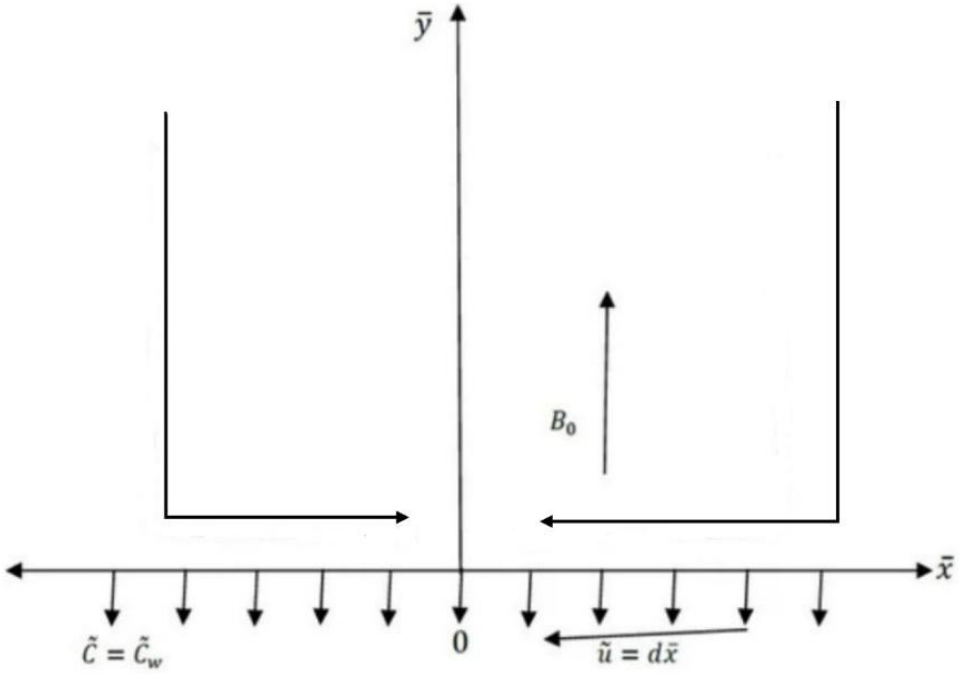

Figure 1. shows the coordinate system and flow problem geometry.

$$\tilde{u}_e(\bar{x}) = a\bar{x}, \;\; \tilde{u}_e(\bar{y}) = a\bar{y}, \tag{1}$$

Here the constant $a > 0$ is proportionality to the free stream velocity apart through the stretched sheet. The consequent boundary layer equations are

$$\frac{\partial \tilde{u}}{\partial \bar{x}} + \frac{\partial \tilde{v}}{\partial \bar{y}} = 0, \tag{2}$$

$$\tilde{u}\frac{\partial \tilde{u}}{\partial \bar{x}}+\tilde{v}\frac{\partial \tilde{u}}{\partial \bar{y}}+\lambda_A\left\{\tilde{u}^2\frac{\partial^2\tilde{u}}{\partial \bar{x}^2}+2\tilde{u}\tilde{v}\frac{\partial^2\tilde{u}}{\partial \bar{x}\,\partial \bar{y}}+\tilde{v}^2\frac{\partial^2\tilde{u}}{\partial \bar{y}^2}\right\}=\nu\frac{\partial^2\tilde{u}}{\partial \bar{y}^2}+$$
$$\tilde{u}_e\frac{d\tilde{u}_e}{d\bar{x}}-\frac{B_0^2\sigma}{\rho}\left[\tilde{u}-\tilde{u}_e+\lambda_A\tilde{v}\frac{\partial\tilde{u}}{\partial\bar{y}}\right]-\frac{\mu}{\rho\bar{k}}\tilde{u} \tag{3}$$

$$\tilde{u}\frac{\partial\tilde{C}}{\partial\bar{x}}+\tilde{v}\frac{\partial\tilde{C}}{\partial\bar{y}}=\bar{D}_B\frac{\partial^2\tilde{C}}{\partial y^2}-k_1\left(\tilde{C}-\tilde{C}_\infty\right), \tag{4}$$

The corresponding BCs are

$$\tilde{u}=\tilde{u}_w(\bar{x})+L_1\frac{\partial\tilde{u}}{\partial\bar{y}}=d\bar{x},\tilde{v}=-\tilde{v}_w,,\tilde{C}=\tilde{C}_w \text{ on } \bar{y}=0, \tag{5}$$

$$\tilde{u}=a\bar{x},\tilde{C}=\tilde{C}_\infty \; at\; \bar{y}\to\infty. \tag{6}$$

In the above equations $\tilde{u},\tilde{v}$ are the velocity constituents alongside the $\bar{x}$ and $\bar{y}$-axis, the relaxation time λ_{11}, the mass diffusion $\bar{D}_B$, the concentration field $\tilde{C}$, d is the stretching rate, and the reaction rate k_1. It is referred (Hayat et al. 2009, Anwar 2020) that the extra expression $\frac{B_0^2\sigma}{\rho}\left[-\tilde{u}_e+\lambda_1\tilde{v}\frac{\partial\tilde{u}}{\partial\bar{y}}\right]$ is in the momentum equation. This investigation embodies alike deduction to the MHD two-phase MHD Maxwell fluid flow in the flourishing explorations.

Defining (Pahlavan et al. 2009, Anwar 2020)

$$\tilde{u}=d\bar{x}G'(\eta),\;\; \tilde{v}=-\sqrt{d\nu}\,G(\eta),\eta=\sqrt{\frac{d}{\nu}}\,\bar{y},\phi(\eta)=\frac{\tilde{C}-\tilde{C}_\infty}{\tilde{C}_w-\tilde{C}_\infty}. \tag{7}$$

where a and d have dimensional reciprocals of time and are positive constants. Equation (2) is similarly satisfied, and Equations (3)–(6) lead to;

$$G'''+\{M\beta_1+1\}GG''-G'^2+\beta_1\{2GG'G''-G^2G'''\}-M(G'-\alpha)-KG'+\alpha^2=0,, \tag{8}$$

$$\phi''+S_cG\phi'-S_cK_c\phi=0, \tag{9}$$

The associated boundary conditions are

$$G'(\eta)=1+\lambda_1G''(\eta),G(\eta)=S,\phi(\eta)=1,\;\; \text{on}\;\; \eta=0, \tag{10}$$

$$G'(\eta)=\alpha,\phi(\eta)=0,\qquad as\;\eta\to\infty, \tag{11}$$

Where $S=\frac{-\bar{v}_0}{\sqrt{a\nu}},\lambda_1=L_1\sqrt{\frac{d}{\nu}},K=\frac{\nu}{\bar{k}d},M=\frac{\sigma\bar{B}_0{}^2}{\rho d},\beta_1=\lambda_Ad,\alpha=\frac{a}{d},S_c=\frac{\nu}{D_B}$ and $K_c=\frac{k_1}{d}$, are the suction, velocity slip parameter, porosity parameter, magnetic parametric quantity, Deborah number, Schmidt number, and chemical reaction parametric quantity respectively. Further, $K_c>0$ or $K_c<0$ stands for destructive or generative chemical reactions, whereas $K_c=0$ stands for non-reactive species.

Physical quantities

Surface skin friction coefficient C_G and local Sherwood number $Sh_{\bar{x}}$ are described as

$$C_G = \frac{2\tau_w}{\rho \tilde{u}_w{}^2}, Sh_{\bar{x}} = \frac{\bar{x} j_w}{D_B\left(\tilde{C}_w - \tilde{C}_\infty\right)}, \tag{12}$$

Where τ_w, the wall shear stress, and m_w mass flux are presented below

$$\tau_w = \mu\left(\frac{\partial \tilde{u}}{\partial \bar{y}}\right)_{\bar{y}=0}, m_w = -D_B\left(\frac{\partial \tilde{C}}{\partial \bar{y}}\right)_{\bar{y}=0} \tag{13}$$

Emplacing Eq. (13) in Eq. (12), gives

$$\frac{1}{2} C_G \sqrt{Re_{\bar{x}}} = G''(0), \frac{Sh_{\bar{x}}}{\sqrt{Re_{\bar{x}}}} = -\phi'(0) \tag{14}$$

Here $Re_{\bar{x}}$ is the local Reynolds number.

Numerical Technique

We implement the Successive Linearization Method (SLM), assuming the expansion (Bhatti et al. 2016, Anwar et al. 2017) given as

$$G(\eta) = G_{i}(\eta) + \sum_{n=0}^{i-1} G_n(\eta), \ (i = 1,2,3, \ldots), \tag{15}$$

Where G_i is the undetermined function to be achieved iteratively. Presuming the earliest hypothesis "G_0" of the mode

$$G_0 = S + \alpha\eta + \frac{1}{1+\lambda_1}(1 - e^{-\eta}). \tag{16}$$

We write Eq. (8) as

$$\mathrm{L} = G''' - M(G' - \alpha) - KG', \tag{17}$$

and

$$\mathrm{N} = \{M\beta_1 + 1\}GG'' + \beta_1\{2GG'G'' - G^2G'''\} - (G')^2 + \alpha^2, \tag{18}$$

L, N are the linear and non-linear segments. By replacing Eq. (15) in Eq. (8) and conceding the linear segment, arrive at

$$G_i''' + C_{0,i-1}G_i''' + C_{1,i-1}G_i'' + C_{2,i-1}G_i' - [M+K]G_i' + C_{3,i-1}G_i + M\alpha = r_{i-1}, \tag{19}$$

The respective boundary conditions become

$$G_i(0) = 0 = G_i'(0) + \lambda_1 G_i'' - 1 = (0) = G_i'(\infty). \tag{20}$$

Eq. (19) is solved through the Chebyshev spectral collocation technique. The conversion of a physical part towards a finite part $[-1,1]$ is brought by applying transformation of the following form;

$$\Gamma = \frac{2\eta-1}{\Theta}. \tag{21}$$

The $[-1,1]$ is discretized. To make the nodal-points into $[-1,1]$, the Gause-Lobatto collocation is utilized i.e.

$$\Gamma_I = \cos\frac{\pi i}{\Gamma}, \ (I = 0,1, \dots N). \tag{22}$$

Holding $(N+1)$ collocation points. The differential matrix "**D**" is the basic theme fundaments of this scheme. Pursuing a differential matrix is further mapping into a vector function $H\left(= [G(\Gamma_0), \dots, G(\Gamma_\Gamma)]^{\boldsymbol{T}}\right)$. The collocation points are specified as

$$H' = \sum_{K=0}^{N} \mathbf{D}_{Ki} G(\Gamma_K) = \mathbf{D}H, \tag{23}$$

the function $G(\Gamma)$ for the q^{th} order derivatives are described as

$$G^q(\Gamma) = \mathbf{D}^q H. \tag{24}$$

The matrix "**D"** is computable utilizing alike strategy conferred by Bhatti et al. (Bhatti et al. 2016, Anwar et al. 2017). Now, the spectral collocation method is employed on linearized Eqs. (19)-(20), arrive at

$$\mathbf{B}_{i-1} H_i = \mathbf{R}_{i-1}, \tag{25}$$

The boundary conditions become

$$G_i(\Gamma_N) = 0, \sum_{K=0}^{N} \mathbf{D}_{NK} G_i(\Gamma_K) = 0, \sum_{K=0}^{N} \mathbf{D}_{\mathbf{0}K} G_i(\Gamma_K) = 0, \sum_{K=0}^{N} \mathbf{D}_{\mathbf{0}K}^{\mathbf{2}} G_i(\Gamma_K) = 0, \tag{26}$$

And

$$\mathbf{B}_{i-1} = \mathbf{D^3} + C_{0,i-1}\mathbf{D^3} + C_{1,i-1}\mathbf{D^2} + C_{2,i-1}\mathbf{D} - (M + \mathrm{K})\mathbf{D} + C_{3,i-1} + M\alpha. \tag{27}$$

where $b_{\mathbb{s},i-1}(\mathbb{s} = 0,1, \dots 3)$ are $(N+1)\times(N+1)$ diagonal matrices along the main diagonal $b_{\mathbb{s},i-1}(\Gamma_N)$,

we have

$$H_i = G_i(\Gamma_I), \mathbf{R}_{i-1} = r_i(\Gamma_I). \ (I = 0,1,2,3, \dots N). \tag{28}$$

The solutions for G_i are attained using Eq. (25) and Eq. (26). Anymore Eq. (9) become linearized, thus Chebyshev pseudo-spectral method is straightforwardly applied, reaching at

$$\mathbb{B} = \mathbb{H}^{-1}\mathbb{S}, \tag{29}$$

$$\phi(\Gamma_N) = 1, \phi(\Gamma_0) = 0, \tag{30}$$

$$\mathbb{B} = \mathbf{D^2} + S_c G\mathbf{D} - S_c K_c \tag{31}$$

where $\mathbb{H} = \phi(\Gamma_I)$. The vectors of zeros are defined by $\mathbb{S}$, and Eqs. (31) is further transformed into the diagonal matrices. Eq. (30) is employed over the foremost and last row of $\mathbb{B}$, and $\mathbb{S}$, subsequently.

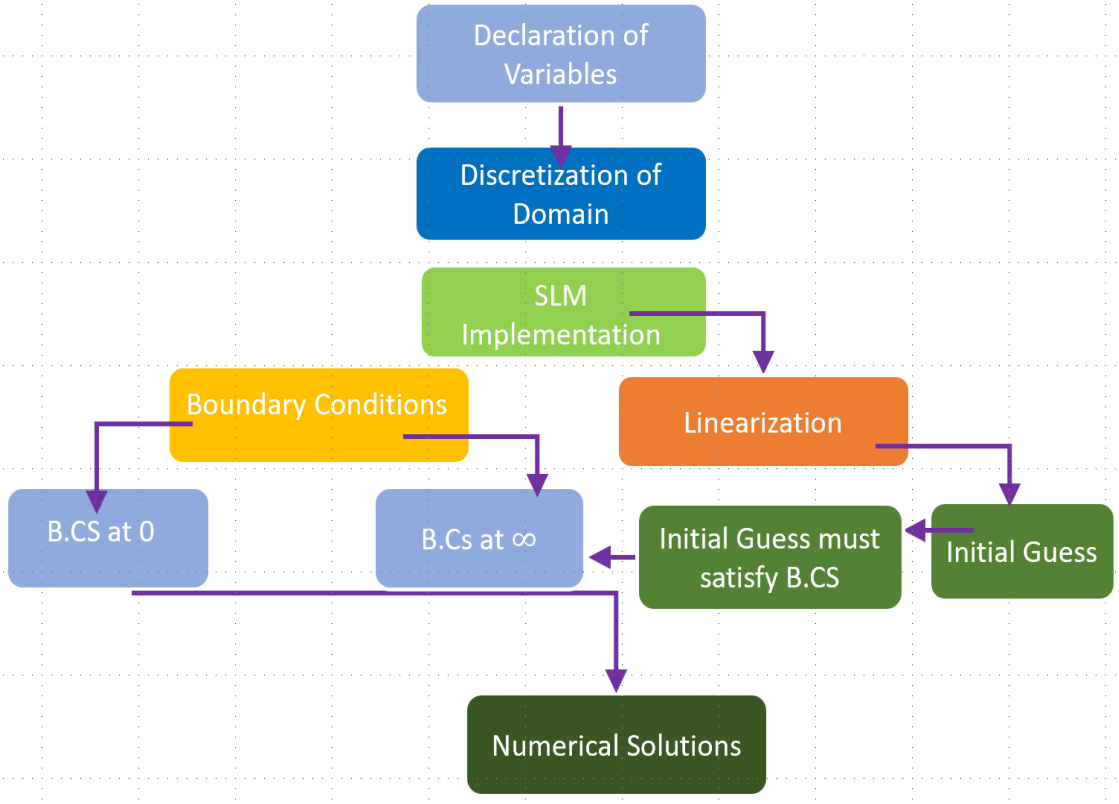

Figure 2: Process flow diagram for generating numerical results

Numerical results and consultation

This segment anticipates the estimated outcomes for the overall parameters contained within the governing equations. The Matlab software has been employed to investigate the anomalies regarding the overall efficacy of the significant parametric variables through numerical analysis. Figures 3-16 are presented to illustrate the significant parametric variables concerning flow profiles, subsequently. In Figures 3-4, the fluctuation in M with respect to velocity and concentration distribution is depicted and documented, revealing that velocity substantially decelerates and diminishes the boundary layer thickness, while concurrently augmenting the concentration magnitudes by increasing the values in M. Through Figures 5-6, the modification in the parameter β_1 for velocity and concentration distribution is illustrated and recorded, indicating that velocity significantly decelerates and elevates the boundary layer thickness, However, it enhances the concentration magnitudes by increasing the values in the parameter β_1. In Figures 7-8, the variation in the parameter α for velocity and concentration distribution is depicted and observed, demonstrating that the velocity field considerably increases and enhances the boundary layer thickness, while simultaneously reducing the concentration magnitudes by elevating the values

in the parameter α. Through Figures 9-10, for the distant numeric in the parameter K, the velocity and concentration distribution are portrayed and revealed, indicating that velocity remarkably decelerates, while the concentration magnitudes are enhanced by augmenting the values in the parameter K. We ascertain through Figures 11-12 that the variation in the parameter S exceptionally decelerates both the velocity and concentration distribution, while also enhancing the boundary layer thickness for elevated amounts in the parameter S. Figure 13 is employed to elucidate the influence of λ_1 on the function $G'(\eta)$profile. It has been determined that $G'(\eta)$ exhibits a noteworthy decline with the elevation of λ_1 values. From a physical standpoint, as the velocity slip parameter escalates, it denotes an augmented slip velocity at the fluid-solid interface, wherein the fluid molecules experience diminished interaction with the solid surface. Consequently, the transfer of momentum between the fluid and the solid surface is attenuated, resulting in a reduction of the velocity profile.

The influence of S_c and K_c on species concentration is shown in Figure 14-16, where both parametric quantities S_c and K_c, slow down the concentration and decelerate the concentration boundary layer thickness. The chemical reaction parameter K_c has a remarkable effect on concentration at the point of chemical reaction that benefits the interface mass transfer; the species concentration decreases for K_c gets large values as being demolishing chemical recedes; by increasing K_c, the concentration magnitudes recorded to be increased for ($K_c < 0$), and it decelerates for ($K_c > 0$). It is important to note that the variation observed for ($K_c < 0$) is significant in comparison to the variation for ($K_c > 0$).

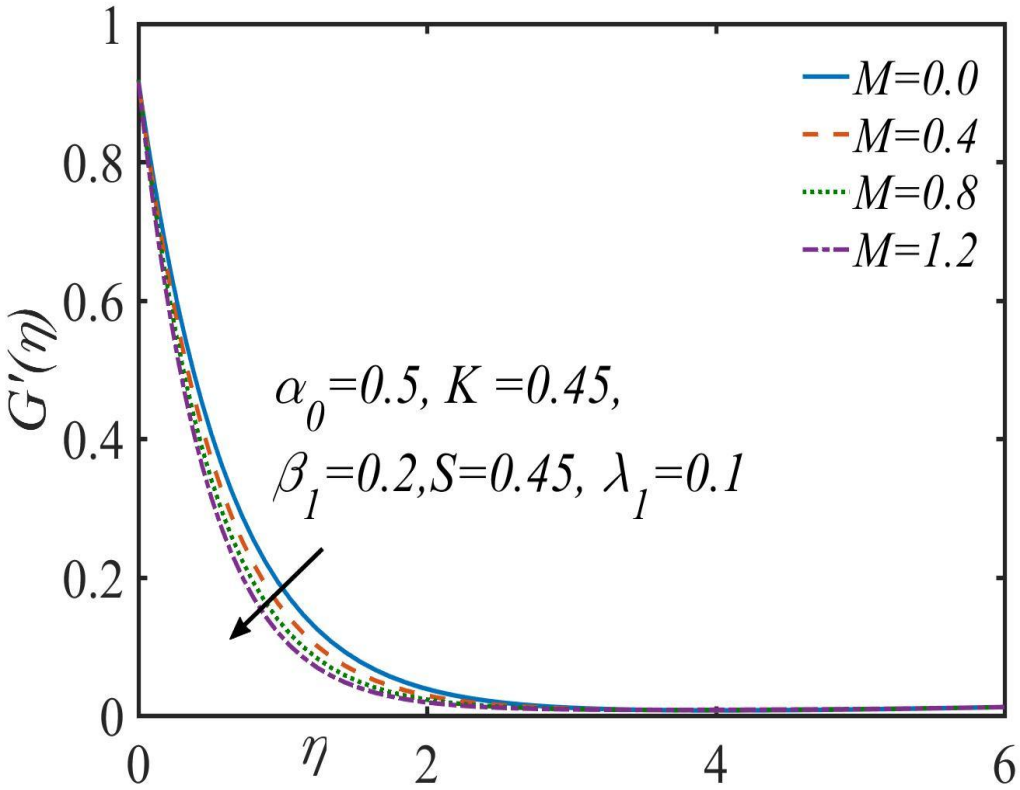

Figure 3: Velocity magnitude for M.

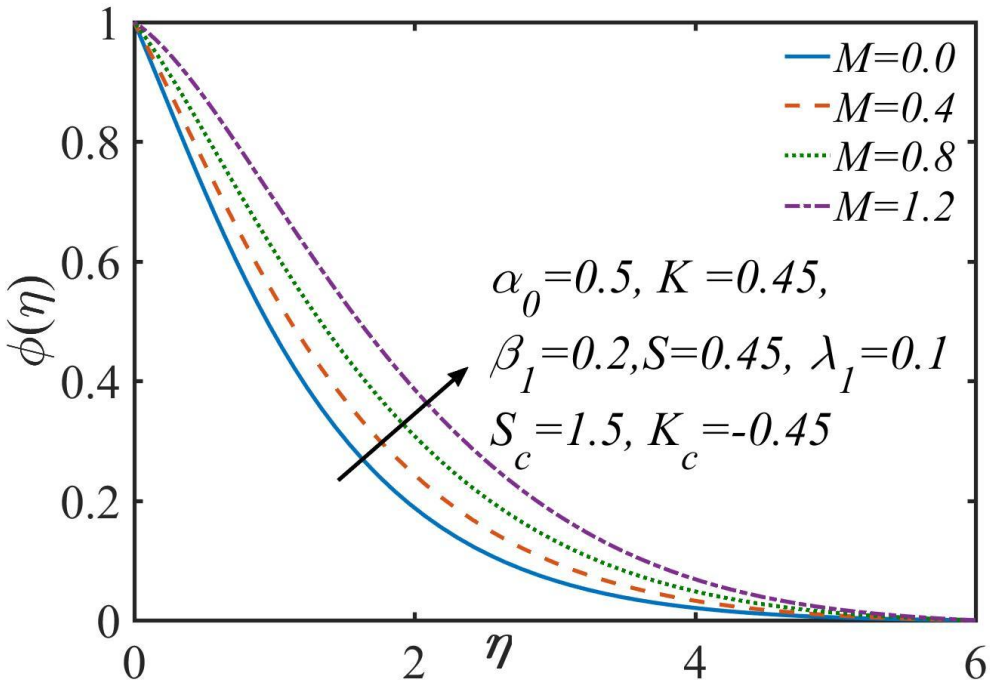

Figure 4: Concentration magnitude for M.

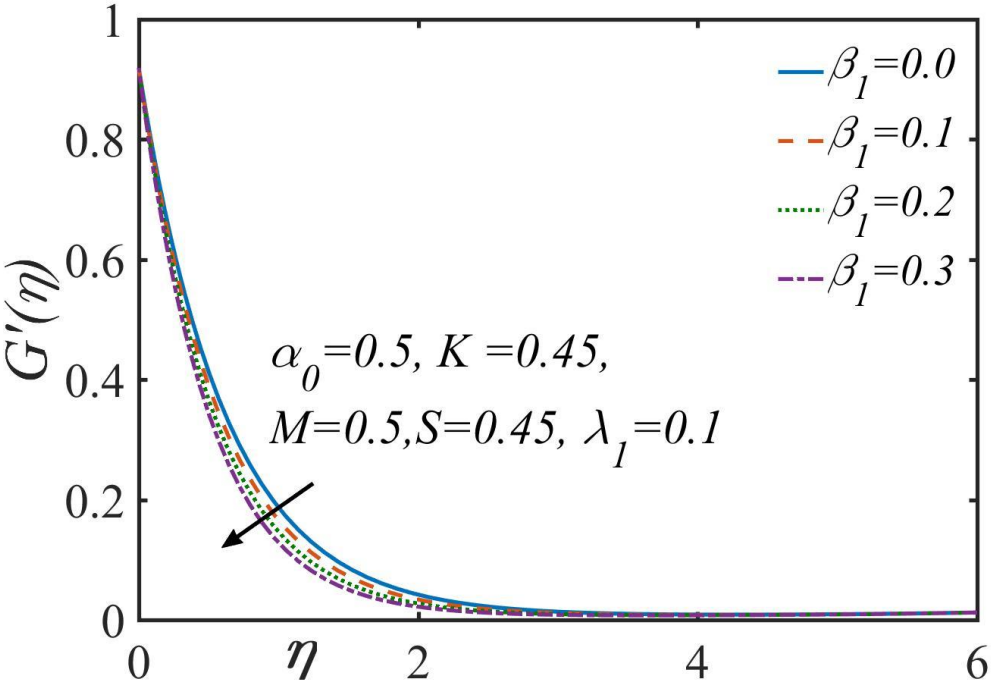

Figure 5: Velocity magnitude for β_1.

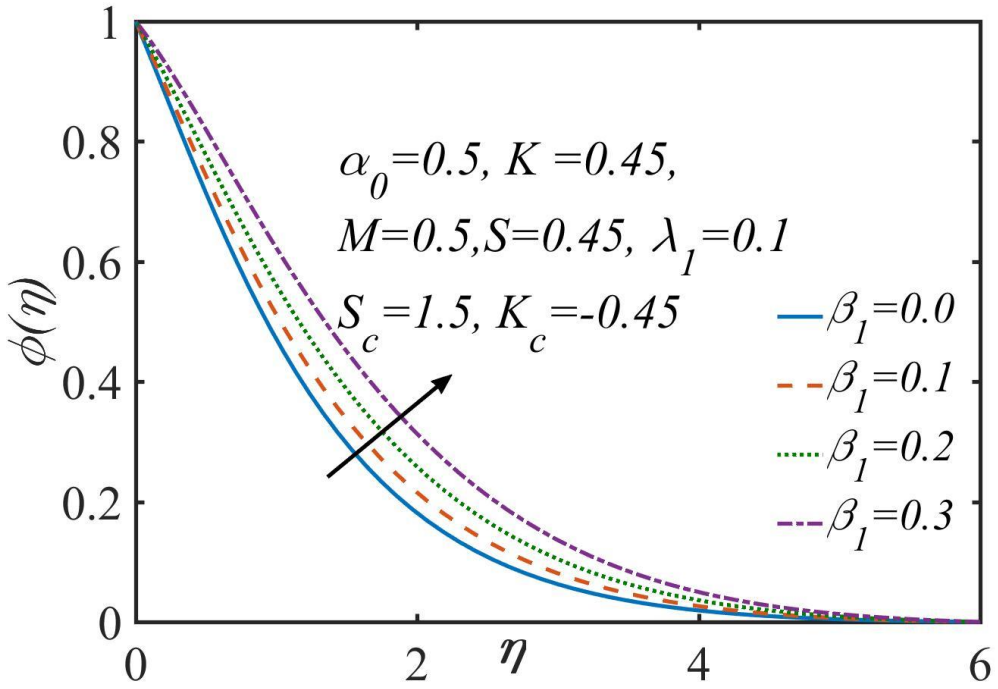

Figure 6: Concentration magnitude for β_1.

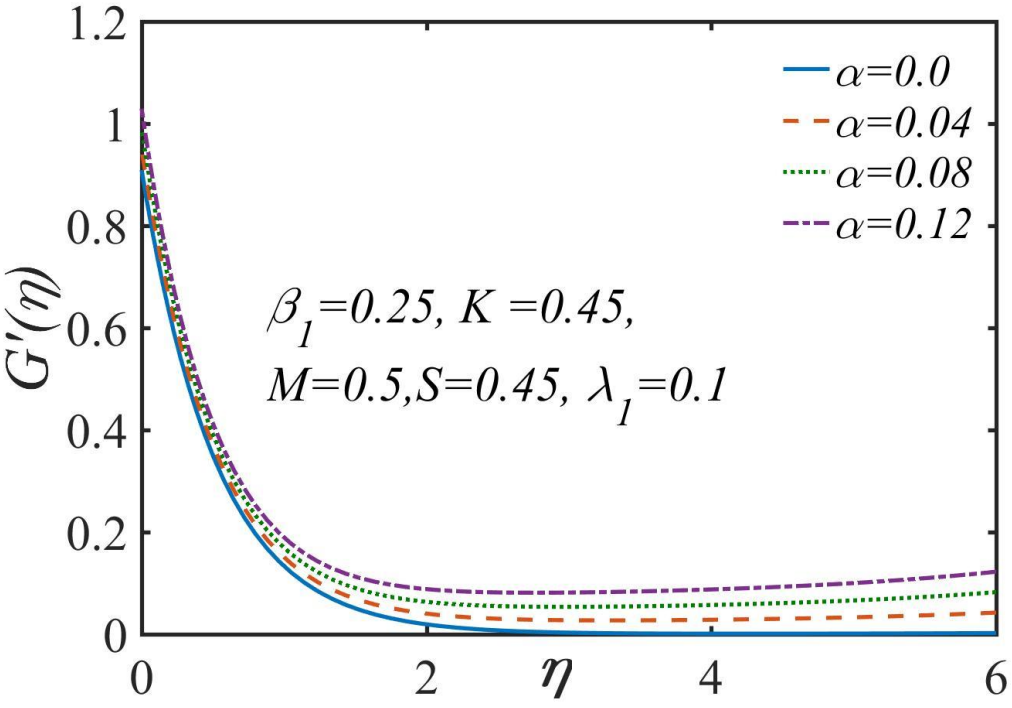

Figure 7: Velocity magnitude for α.

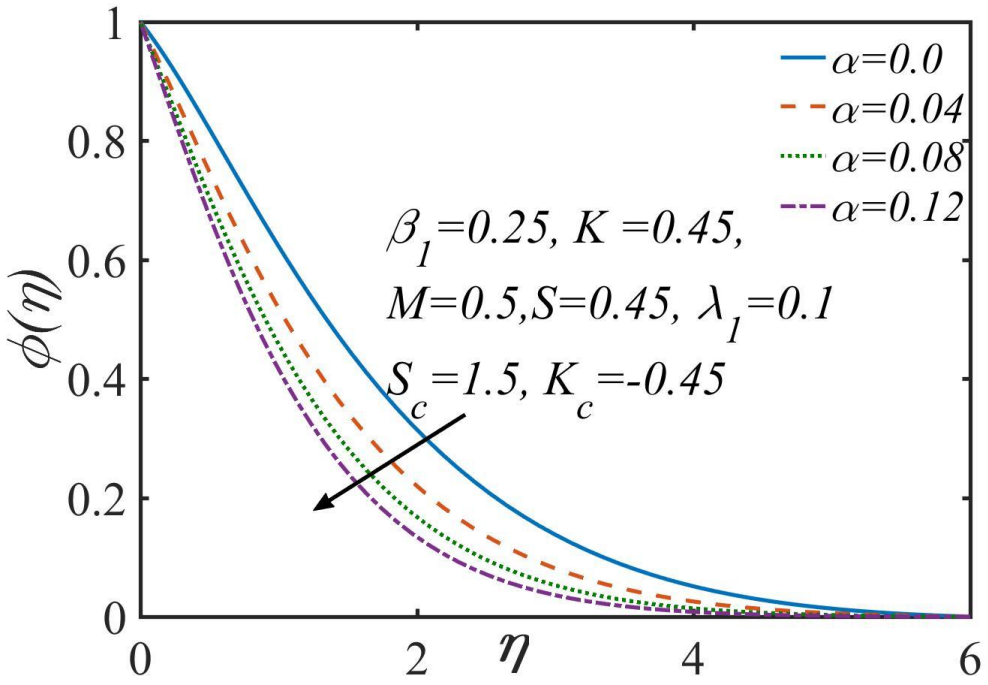

Figure 8: Concentration magnitude for α.

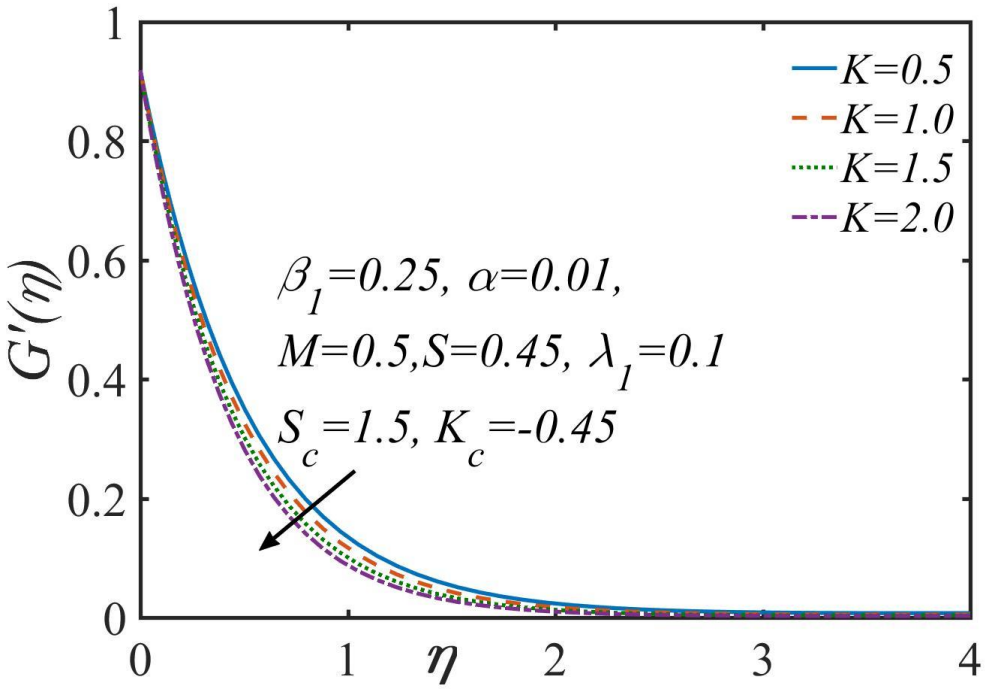

Figure 9: Velocity magnitude for K.

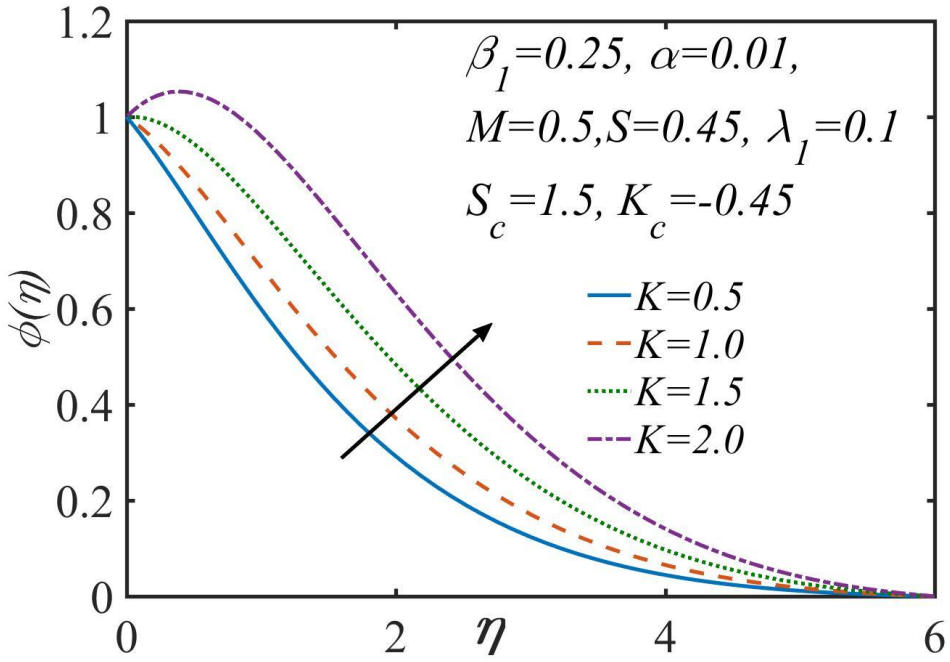

Figure 10: Concentration magnitude for K.

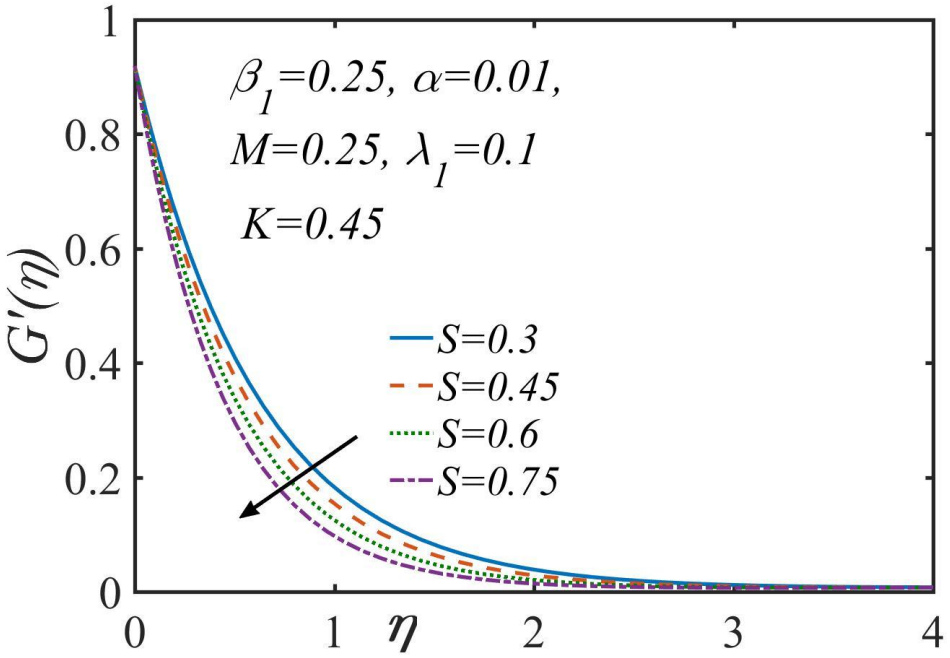

Figure 11: Velocity magnitude for S.

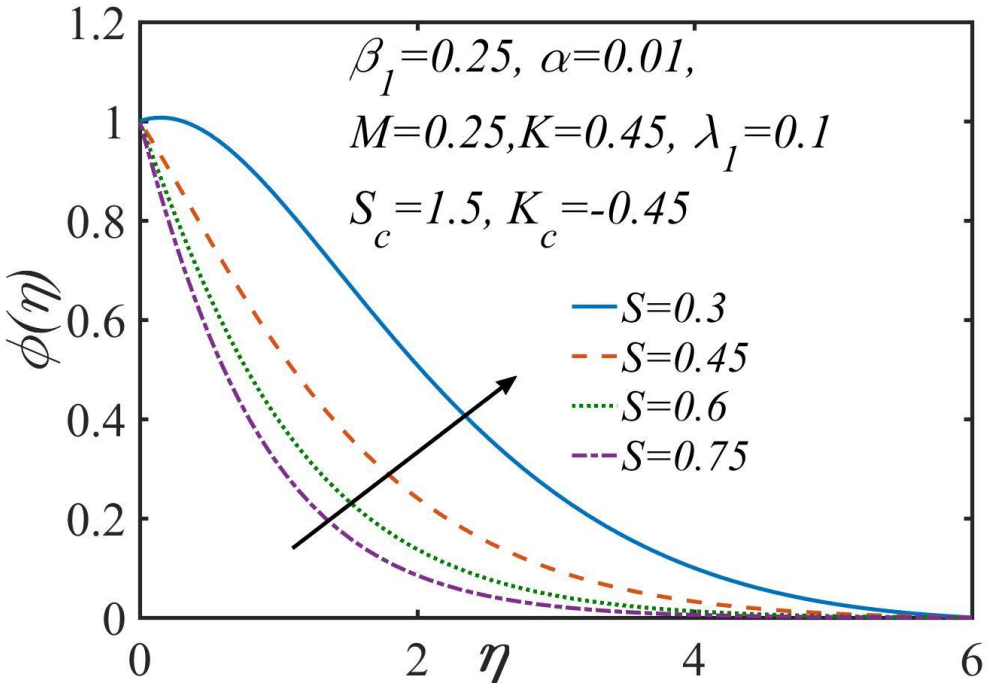

Figure 12: Concentration magnitude for S.

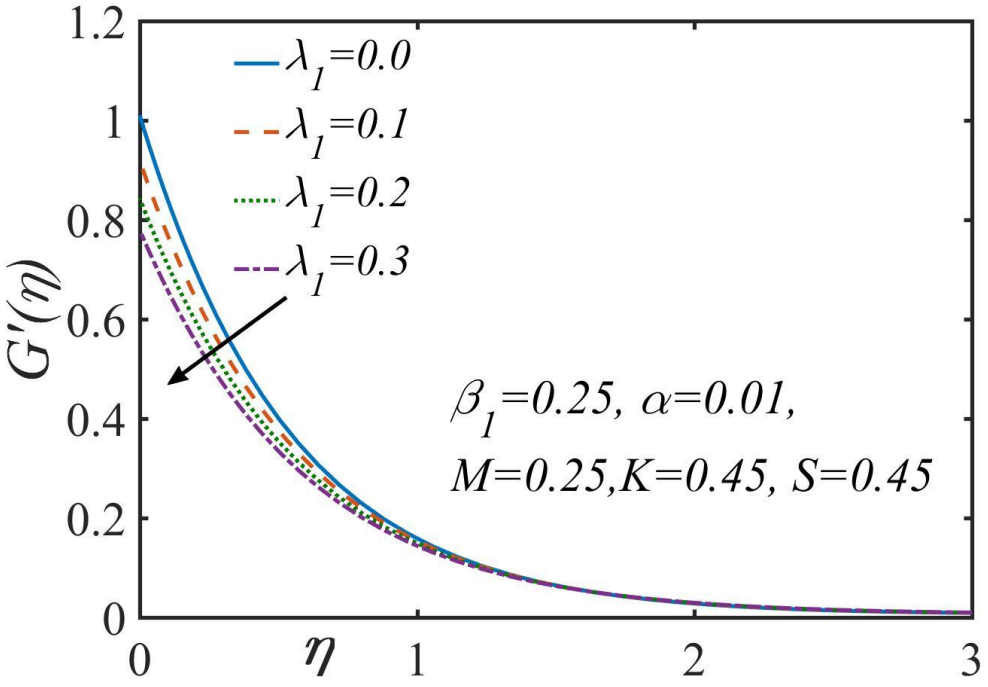

Figure 13: Velocity magnitude for λ_1.

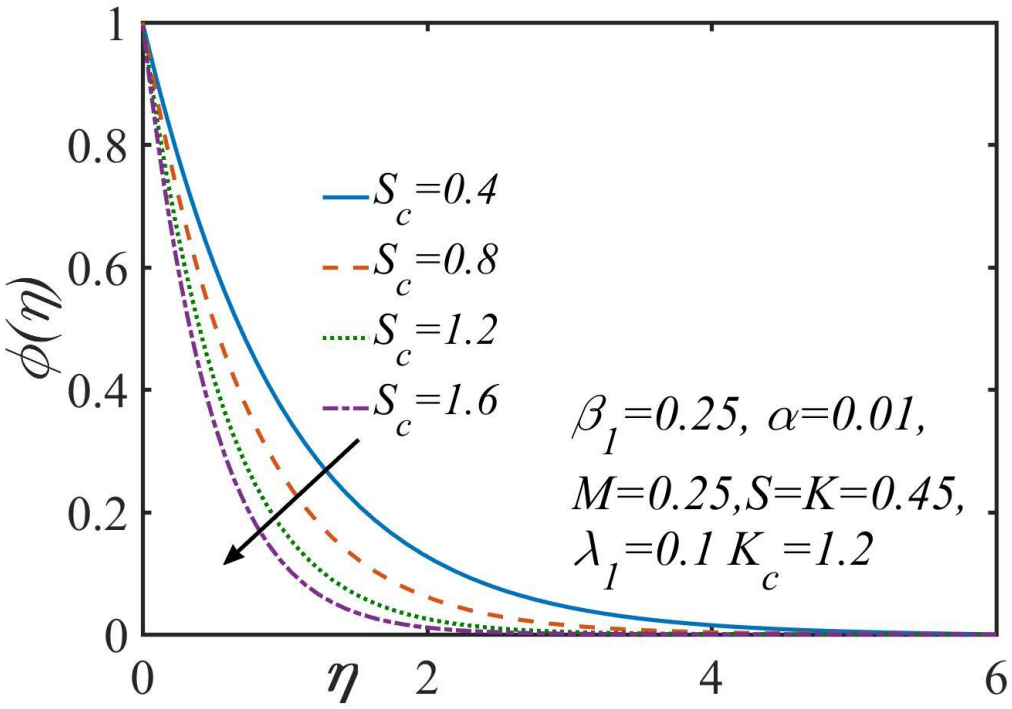

Figure 14: Concentration magnitude for S_c.

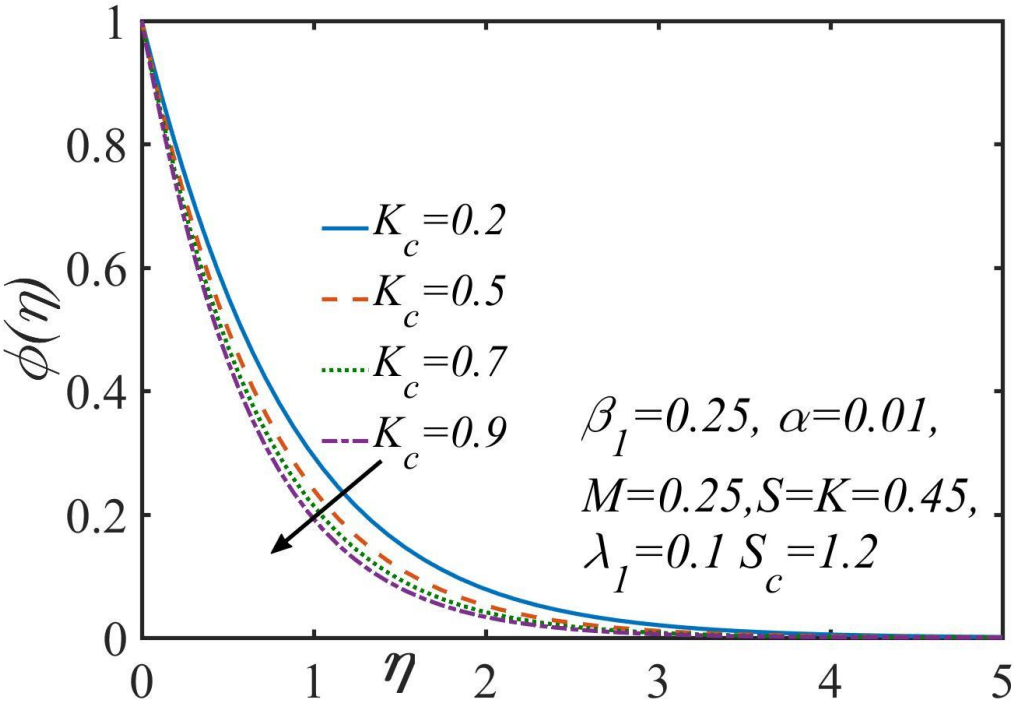

Figure 15: Concentration magnitude for $K_c \geq 0$.

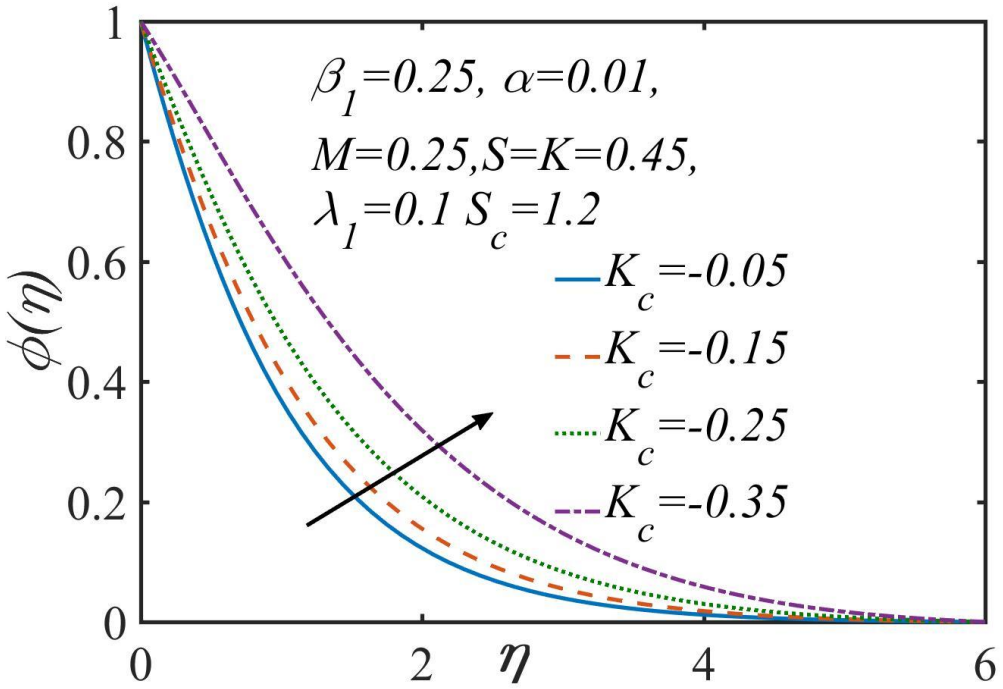

Figure 16: Concentration magnitude for $K_c < 0$.

To evaluate the precision of the numerical methodology employed, the results are juxtaposed with the extant literature provided by Pahlavan et al. 2009 and Anwar 2020. It has been noted that the results yielded by the SLM method exhibit a higher degree of accuracy as delineated in Table 1.

Table 1: Comparison of current results of $G''(0)$ and $-\phi'(\eta)$ with the previous investigations across S_c and K_c by fixing $M = 1, \beta_1 = \alpha = 0.2, K = S = \lambda_1 = 0$.

S_c	K_c	Current Results for $G''(0)$	Pahlavan et al. 2009 and Anwar 2020	Current Results for $-\phi'(\eta)$	Pahlavan et al. 2009 and Anwar 2020
1	1	1.272470	1.272470	1.167862	1.16786
1.2	1			1.284681	1.28468
1.5	1			1.443482	1.44348
1	1.2			1.252273	1.25227
1	1.5			1.368854	1.36885

Conclusion

The present investigation elucidates the effects of velocity slip and mass transfer on the flow of MHD upper-convected Maxwell (UCM) fluids over a stretched permeable plate near the stagnation point. The governing partial differential equations associated with the flow issue are transformed into ordinary differential equations through the application of similarity transformations. The numerical results for the ascending non-linear boundary

value problem are ascertained through the execution of the Successive Linearization Method (SLM) utilizing Matlab software. The subsequent observations are documented as follows:

The alteration in M for the velocity distribution significantly retards while simultaneously amplifying the concentration magnitude.

- The alteration in β_1 decelerates the velocity profile, although intensifying the concentration magnitudes.
- The alteration in α markedly increases the velocity magnitudes while concurrently decelerating the concentration magnitudes.
- An increase in numeric in K results in a deceleration of the distribution while enhancing the concentration magnitudes.
- By augmenting S, there is a notable deceleration in both velocity and concentration distributions.
- The concentration magnitudes progressively decelerate across both parametric quantities S_c and K_c.
- The concentration field exhibits contradictory behavior across $((K_c > 0)$ and $(K_c < 0)$.
- Slip conditions pertain to the differential motion or velocity disparity between the fluid and the boundary at the interface of fluid and solid. The examination of various slip phenomena can yield numerous implications across diverse disciplines: microfluidics, nanofluidics, transport in porous media, tribology, thin liquid films, biological systems, aerospace, and aeronautics, among others. The subsequent points are duly noted.

Declaration

Acknowledgment: N/A

Funding: This research received no external funding.

Conflict of interest: The author declares no conflict of interest.

Ethics approval/declaration: All ethics of paper publications were observed

Consent to participate: The author participated in writing this paper

Consent for publication: The author consented to the publication of this paper

Data availability: N/A

Author contribution: The author contributed to the whole

References

Anwar, T.; Kumam, P.; Watthayu, W. Influence of Ramped Wall Temperature and Ramped Wall Velocity on Unsteady Magnetohydrodynamic Convective Maxwell Fluid Flow. *Symmetry* 2020, *12*, 392.

Shah, Z.; Alzahrani, E.; Jawad, M.; Khan, U. Microstructure and Inertial Characteristics of MHD Suspended SWCNTs and MWCNTs Based Maxwell Nanofluid Flow with Bio-Convection and Entropy Generation Past a Permeable Vertical Cone. *Coatings* 2020, *10*, 998.

Ahmed, J.; Khan, M.; Ahmad, L. MHD swirling flow and heat transfer in Maxwell fluid driven by two coaxially rotating disks with variable thermal conductivity. *Chin. J. Phys.* 2019, *60*, 22–34.

Chen, X.H.; Yang, W.D.; Zhang, X.R.; Liu, F.W. Unsteady boundary layer flow of viscoelastic MHD fluid with a double fractional Maxwell model. *Appl. Math. Lett.* 2019, *95*, 143–149.

Shehzad, S.A.; Mabood, F.; Rauf, A.; Tlili, I. Forced convective Maxwell fluid flow through rotating disk under the thermophoretic particles motion. *Int. Commun. Heat Mass Transf.* 2020, *116*, 104693.

S. Ullah, I. Ullah, A. Ali, K. Shah, T. Abdeljawad, Investigation of cross-diffusion effect on radiative Jeffery-Hamel flow in convergent/divergent stretchable channel with Lorentz force and Joule heating, Alex. Eng. J., (2024). 86: 289-297

A., Shahid, H., Huang, M. M., Bhatti, L., Zhang, & R. Ellahi, Numerical investigation on the swimming of gyrotactic microorganisms in nanofluids through porous medium over a stretched surface. *Mathematics*, (2020), *8*(3): 380.

A. Shahid, W. Wei, M. M. Bhatti, O. A. Bég, T. A. Bég, Mixed convection Casson polymeric flow from a nonlinear stretching surface with radiative flux and non-Fourier thermal relaxation effects: Computation with CSNIS, ZAMM - *Journal of Applied Mathematics and Mechanics*, (2023). 103(10): https://doi.org/10.1002/zamm.202200519.

Y.S. Daniel, Z.A. Aziz, Z. Ismail, F. Salah, Entropy analysis in electrical magnetohydrodynamic (MHD) flow of nanofluid with effects of thermal radiation, viscous dissipation, and chemical reaction, *Theoretical and Applied Mechanics Letters*, (2017), 7 (4) : 235–242.

V.R. Mulinti, L. Pallavarapu, Influence of thermal radiation and viscous dissipation on MHD flow of UCM fluid over a porous stretching sheet with higher order chemical reaction, *Spec. Top Rev. Porous Media Int. J.*, (2022), 12 (4):

A. Wakif, A. Abderrahmane, K. Guedri, B. Bouallegue, R. Kaewthongrach, P. Kaewmesri, A. Jirawattanapanit, Importance of exponentially falling variability in heat generation on chemically reactive von k´ arm´ an nanofluid flows subjected to a radial magnetic field and controlled locally by zero mass flux and convective heating conditions: a differential quadrature analysis, *Frontiers in Physics*, (2022), 768:

Vinodkumar M. Reddy, P. Lakshminarayana, Higher order chemical reaction and radiation effects on magnetohydrodynamic flow of a maxwell nanofluid with Cattaneo–Christov heat flux model over a stretching sheet in a porous medium, *J. Fluid Eng.*, (2022), 144 (4): 041204.

S.D. Yahaya, U. Aliyu, H. Umaru, Stagnation point flow with thermal and magnetic field over a stretching sheet, *Sci. World J.*, (2022), 17 (2): 191–199.

U.S. Mahabaleshwar, K.N. Sneha, A. Wakif, Significance of Thermo-Diffusion and Chemical Reaction on MHD Casson Fluid Flows Conveying CNTs over a Porous Stretching Sheet. *Waves in Random and Complex Media*, (2023), 1–19.

M.I. Anwar, H. Firdous, A.A. Zubaidi, N. Abbas, S. Nadeem, Computational analysis of induced magnetohydrodynamic non-Newtonian nanofluid flow over nonlinear stretching sheet, *Prog. React. Kinet. Mech.*, 47 (2022), 14686783211072712.

H.T. Alkasasbeh, A. Abderrahmane, A. Mourad, K. Guedri, E.M. Tag, O. Younis, Analysis of 3-D MHD maxwell hybrid nanofluid flow over a stretching sheet, *Heliyon*, (2023), 4376147, https://doi.org/10.2139/ssrn.4376147, 1-23.

A., Shahid, H.L., Huang, M.M. Bhatti, and M., Marin, Numerical computation of magnetized bioconvection nanofluid flow with temperature-dependent viscosity and Arrhenius kinetic. *Mathematics and Computers in Simulation.*, (2022), 200, 377-392.

N. Elboughdiri, D. Ghernaout, T. Muhammad, A. Alshehri, R. Sadat, M.R. Ali, A. Wakif, Towards a novel EMHD dissipative stagnation point flow model for radiating copper-based ethylene glycol nanofluids: an unsteady two-dimensional homogeneous second-grade flow case study, *Case Stud. Therm. Eng.*, (2023), 45: 102914.

Makinde, O.D. MHD mixed-convection interaction with thermal radiation and nth-order chemical reaction past a vertical porous plate embedded in a porous medium. *Chem. Eng. Commun.* 2011, *198*, 590–608.

Beg, O.A.; Makinde, O.D. Viscoelastic flow and species transfer in a Dacian high-permeable channel. *J. Petrol. Sci. Eng.* 2011, *76*, 93–99.

Abbas, M.A.; Bhatti, M.M.; Sheikholeslami, M. Peristaltic Propulsion of Jeffrey Nanofluid with Thermal Radiation and Chemical Reaction Effects. *Inventions* 2019, *4*, 68.

Khan, W.A.; Culham, J.R.; Makinde, O.D. Combined heat and mass transfer of third-grade nanofluids over a convectively-heated stretching permeable surface. *Can. J. Chem. Eng.* 2015, *93*, 1880–1888.

Deebani, W.; Tassaddiq, A.; Shah, Z.; Dawar, A.; Ali, F. Hall Effect on Radiative Casson Fluid Flow with Chemical Reaction on a Rotating Cone through Entropy Optimization. *Entropy* 2020, *22*, 480.

Al-Khaled, K.; Khan, S.U. Thermal Aspects of Casson Nanoliquid with Gyrotactic Microorganisms, Temperature-Dependent Viscosity, and Variable Thermal Conductivity: Bio-Technology and Thermal Applications. *Inventions* 2020, *5*, 39.

Makinde, O.D.; Sibanda, P. Effects of chemical reaction on boundary layer flow past a vertical stretching surface in the presence of internal heat generation. *Int. J. Numer. Meth. Heat Fluid Flow* 2011, *21*, 779–792.

Eid, M.R.; Mahny, K.L. Unsteady MHD heat and mass transfer of a non-Newtonian nanofluid flow of a two-phase model over a permeable stretching wall with heat generation/absorption. *Adv. Powder Technol.* 2017, *28*, 3063–3073.

Reddy, P.S.; Sreedevi, P.; Chamkha, A.J. Magnetohydrodynamic (MHD) boundary layer heat and mass transfer characteristics of nanofluid over a vertical cone under convective boundary condition. *Propuls. Power Res.* 2018, *7*, 308–319.

M. M. Bhatti, M. A. Abbas, & M. M. Rashidi, A robust numerical method for solving stagnation point flow over a permeable shrinking sheet under the influence of MHD. Applied Mathematics and Computation, 316: (2018), 381-389.

M. M. Bhatti, A. Shahid, MM, Rashidi, Numerical Simulation of Fluid flow over a shrinking porous sheet by Successive linearization method, Alexandria Eng J., 55: (2016), 51-56.

A. Shahid, M. M. Bhatti, O.A. Beg, A. Kadir, Numerical Study of Radiative Maxwell Viscoelastic Magnetized Flow from a Stretching Permeable Sheet with the Cattaneo-Christov Heat Flux Model, Neural Comput. Appl., 9: (2017), 1-12.

A. Shahid, Z. Zhou, M. Hassan, M. M. Bhatti, Computational Study of Magnetized Blood Flow in the Presence of Gyrotactic Microorganisms Propelled through Permeable Capillary in a Stretching Motion, International Journal for Multiscale Computational Engineering, 16(4): (2018), 303-320.

T. Hayat, Z. Abbas, M. Sajid, MHD stagnation-point flow of an upper-convected Maxwell fluid over a stretching surface, Chaos, Solitons and Fractals, 39: (2009), 840–848.

The Effectiveness of Mass Transfer in the MHD Upper-Convected Maxwell Fluid Flow on a Stretched Porous Sheet near Stagnation Point: A Numerical Investigation, *Inventions*, 2020, *5*(4), 64; https://doi.org/10.3390/inventions5040064.

A.A. Pahlavan, V. Aliakbar, F.V. Farahani, K. Sadeghy, MHD flows of UCM fluids above porous stretching sheets using two-auxiliary-parameter homotopy analysis method, Comm. Nonlinear Sci. Numer. Simulat., 14: (2009), 473–488.